Tuning the course of evolution on the biophysical fitness landscape of an RNA virus

Assaf Rotem[1,#], Adrian W.R. Serohijos[2,10,#], Connie B. Chang[1,9], Joshua T. Wolfe[3], Audrey E. Fischer[3], Thomas S. Mehoke[3], Huidan Zhang[1,4], Ye Tao[1], W. Lloyd Ung[1], Jeong-Mo Choi[2], Abimbola O. Kolawole[5], Stephan A. Koehler[1], Susan Wu[3], Peter M. Thielen[3], Naiwen Cui[1], Plamen A. Demirev[3], Nicholas S. Giacobbi[6], Timothy R. Julian[7,12], Kellogg Schwab[7], Jeffrey S. Lin[3], Thomas J. Smith[8], James M. Pipas[6], Christiane E. Wobus[5], Andrew B. Feldman[11], David A. Weitz[1,*], and Eugene I. Shakhnovich[2,*]

[1] School of Engineering and Applied Sciences and Department of Physics, Harvard University, 9 Oxford Street, Cambridge, MA 02138, USA
[2] Department of Chemistry and Chemical Biology, Harvard University, 12 Oxford Street, Cambridge, MA 02138, USA
[3] Johns Hopkins University Applied Physics Laboratory, 11100 Johns Hopkins Road, Laurel, MD 20723, USA
[4] Department of Cell Biology, Key Laboratory of Cell Biology, Ministry of Public Health, and Key Laboratory of Medical Cell Biology, Ministry of Education, China Medical University, Shenyang 110001, China
[5] Department of Microbiology and Immunology, University of Michigan Medical School, 1150 West Medical Center Drive, Ann Arbor, MI 48109, USA
[6] Department of Biological Sciences, University of Pittsburgh, 4249 Fifth Avenue, Pittsburgh, PA 15260, USA.
[7] Environmental Health Sciences and the Hopkins Water Institute, Johns Hopkins Bloomberg School of Public Health , Baltimore, Maryland 21231, USA
[8] Department of Biochemistry and Molecular Biology, University of Texas Medical Branch at Galveston, 301 University Boulevard, Galveston, TX 77555, USA
[9] Chemical and Biological Engineering Department, Montana State University, Bozeman, Montana, USA
[10] Département de Biochimie et Centre Robert-Cedergren en Bioinformatique et Génomique, Université de Montréal, Quebec, Canada
[11] Department of Emergency Medicine, Johns Hopkins Medicine, 5801 Smith Avenue, Suite 3220, Davis Building, Baltimore, MD, 21209, USA
[12] Department of Environmental Microbiology, Swiss Federal Institute of Aquatic Science and Technology (Eawag), 8600 Dübendorf, Switzerland.

[#]These authors contributed equally.
*Corresponding authors:
D.A.W. (weitz@seas.harvard.edu)
E.I.S. (shakhnovich@chemistry.harvard.edu)

ABSTRACT

Predicting viral evolution remains a major challenge with profound implications for public health. Viral evolutionary pathways are determined by the fitness landscape, which maps viral genotype to fitness. However, a quantitative description of the landscape and the evolutionary forces on it remain elusive. Here, we apply a biophysical fitness model based on capsid folding stability and antibody binding affinity to predict the evolutionary pathway of norovirus escaping a neutralizing antibody. The model is validated by experimental evolution in bulk culture and in a drop-based microfluidics device, the "Evolution Chip", which propagates millions of independent viral sub-populations. We demonstrate that along the axis of binding affinity, selection for escape variants and drift due to random mutations have the same direction. However, along folding stability, selection and drift are opposing forces whose balance is tuned by viral population size. Our results demonstrate that predictable epistatic tradeoffs shape viral evolution.

INTRODUCTION

Responding to viral pandemics or to the emergence of new microbial pathogens is a major challenge to public health (Taubenberger et al., 2007). A critical component to this response is the prediction of the course of microbial evolution. One approach to this prediction uses available genomic samples and branching patterns of genealogical trees to statistically project future dominant strains (Luksza and Lassig, 2014). However, this approach can only infer the likelihood that an existing viral strain will dominate, and cannot predict emergence of novel strains that might become dominant due to *de novo* beneficial mutations. It is these novel strains that are often the most virulent, posing the greatest hazard to public health. Predicting the evolution of novel strains is the key to addressing this challenge and requires knowledge of the relationship between mutations in the viral genome and the fitness for individual organisms (de Visser and Krug, 2014). This relationship is the fitness landscape, which is a complex, multidimensional function; however, this can rarely be quantitatively determined. Nevertheless, it is essential for predicting selection of the most probable mutants. Moreover, the fate of mutations is also a function of population structure (Kimura, 1968). In particular, population size

changes the balance between the impact of random mutations on fitness and that of selection (Lynch and Conery, 2003) and is thought to affect both the rate and direction of evolution (Wright, 1931). Recent studies use microbial fitness landscapes (Acevedo et al., 2014; Gong et al., 2013; Sanjuan et al., 2004) or population structure (Lang et al., 2013; Nahum et al., 2015) to predict the course of evolution, but to date, none links these elements together. Without this link, further progress in predicting the course of viral evolution is significantly hindered.

In this paper, we quantitatively determine a fitness landscape for an RNA virus subjected to the environmental pressure of a neutralizing antibody, and use it to account for the evolution of the virus under conditions that constrain population size. The experimentally measured fitness landscape is correctly described by two biophysical parameters: the thermodynamics of folding of the capsid protein and its binding to the antibody. We probe the evolution of a model norovirus both in bulk, where population size is large, and in a microfluidic evolution chip which uses small drops to perform millions of experiments (Fischer et al., 2015; Guo et al., 2012; Tao et al., 2015a; Tao et al., 2015b; Zhang et al., 2015) that probe evolution in very small population sizes. We show that the dynamics of viral adaptation is strongly dependent on population size. These results can be quantitatively described by a theoretical framework that combines protein biophysics and population genetics, providing the critical link between fitness landscape and population structure that enables prediction of evolution.

We focus in this work on Murine Norovirus (MNV), a model for human RNA viruses which are the major cause of epidemics in the world (Ettayebi et al., 2016; Jones et al., 2014; Wobus et al., 2006). MNV is a non-enveloped RNA virus that consists of 180 copies of the capsid protein assembled around a 7.5kb long positive-strand RNA genome. It mutates at ~1 base per genome per replication cycle and produces ~10^4 progenies in a single cell infection, of which ~100 are infectious viral particles, or plaque forming units (pfu)(Fischer et al., 2015).

RESULTS

To study viral evolution, we propagate a viral isolate (MNV-1, denoted *wt*) in the presence of a neutralizing antibody (mAb6.2, (Kolawole et al., 2014b)) that binds to the protruding domain (P-domain) of the capsid, and prevents virus entry into the host cell (Katpally et al., 2008; Taube et al., 2010). This set-up allows us to study the way the virus evolves to adapt to a new

environment. To investigate the dynamics of this escape from the antibody, we sequence a 376 bp fragment of the genome encoding the outermost part of the P-domain (residues 281 – 412 of VP1) and follow the frequency of 37,244 unique haplotypes (Fig. S1 and Table S1) observed over several passages, allowing us to follow the evolution over several generations. First, we propagate *wt* in standard bulk culture conditions, using ~10^6 virions per passage under Ab pressure (Fig. 1A). The population is initially dominated by the *wt* (~90% of the population) with the rest of the viral quasi-species consisting of single and double mutants (Table S1). After 2 passages the total number of surviving viruses has decreased significantly due to the neutralizing effect of the Ab (Fig. S2); however, three single mutants E296K (*A*), D385G (*B*), T301I (*C*) as well as their double mutants (*AB*, *AC*, *BC*) occur at higher frequencies than the other haplotypes. By the fourth passage the triple mutant *ABC*, which first arises on passage 2, occurs at a frequency even higher than the other mutant haplotypes (86%); moreover, the total number of viruses increases to levels comparable to those observed after the first passage (Fig S2). This suggests that *ABC* is an escape variant.

A central tenet of evolutionary theory is that the way organisms explore their fitness landscape depends on the size of their population, which controls the balance between random mutational drift (i.e., direction of *randomly arising* mutations) in the population and fitness driven selection (i.e., direction of beneficial mutations) (Kimura, 1968; Lynch and Conery, 2003). This balance determines the most likely evolutionary pathways on a given fitness landscape. Indeed, the population size may be particularly important for noroviruses where a single viral particle is sufficient to infect the host animal (Teunis et al., 2008); thus it is possible that viruses propagate in very small populations as they adapt to a new environment prior to the emergence of an epidemic.

The consequences of a smaller population size are captured by the shifting balance theory of Wright (Wright, 1931), which hypothesizes that evolution can proceed more efficiently in three phases: i) a population is divided into subpopulations to weaken selection and increase drift, ii) each subpopulation evolves independently, whereupon iii) the subpopulations are mixed back into a large population and then all individuals compete. We can directly probe this hypothesis experimentally by drastically reducing population size compared to typical laboratory bulk cultures, which propagate ~10^6 to 10^8 viruses (Fig. S2). To evolve viruses in small population

sizes we use a novel microfluidics system, the "Evolution Chip", which propagates ~10^6 subpopulations of 1-10 infectious particles (pfu) in distinct and non-mixing compartments (Fig. 1B, Fig. S3 Movie S1 and Movie S2). The microfluidics system allows us to drastically reduce the population size without reducing the total number of viruses sampled, thereby maintaining the statistics comparable to that of a bulk experiment.

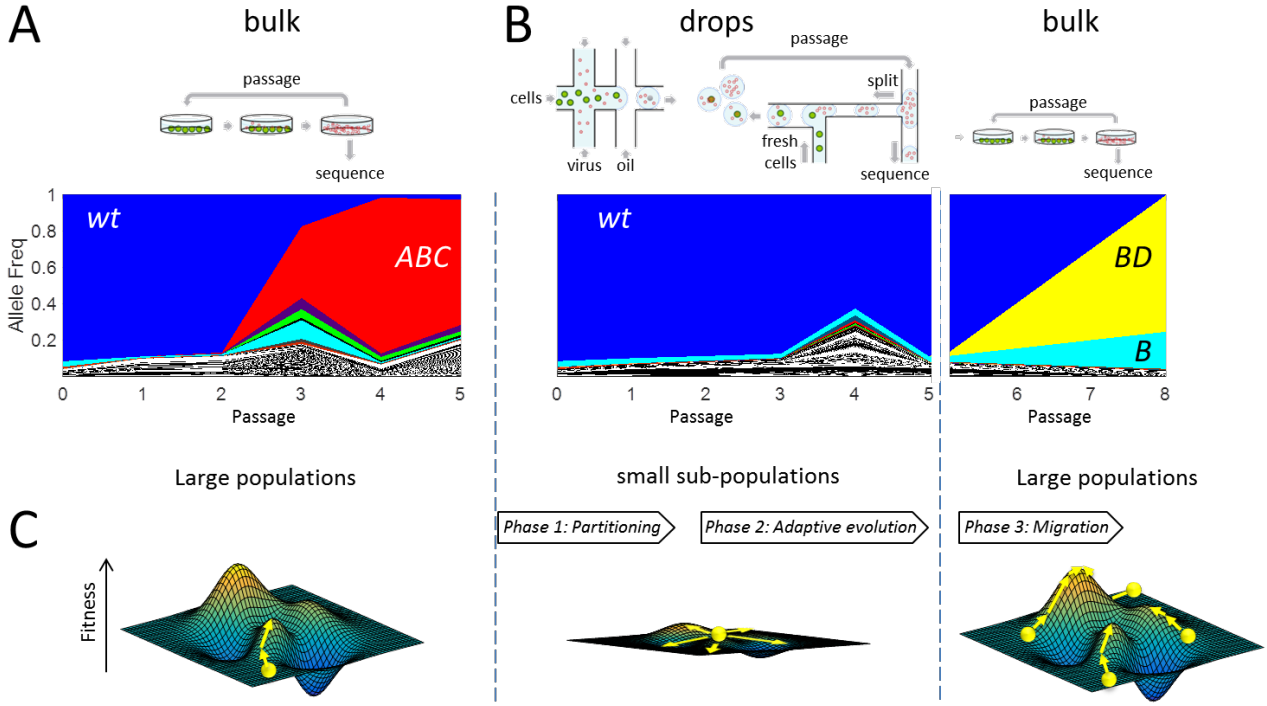

Figure 1. Wright's shifting balance theory (SBT) - Viral evolution in large and small population sizes. A) Top: 10^6 viruses evolving against a neutralizing antibody in bulk by serial propagation. **Bottom:** The allele frequencies of 1,364 distinct P-domain haplotype sequences are plotted per passage (see also Fig. S6**). B) Viral evolution in small populations. Top:** Experimental scheme of the three phases of Wright's SBT - *Phase 1*: 10^6 pico-liter drops are loaded with on average 1 virus and 2 host cells per drop. *Phase 2:* viruses evolve in drops for five passages. *Phase 3:* the emulsion is broken and all lineages evolve together in bulk for 3 additional passages (frequencies for passages 6 and 7 are interpolated from passages 5 and 8, see also , Fig. S5 and Movie S1, S2). **Bottom:** The allele frequencies of 620 distinct P-domain haplotypes from B (*Phase 2, center panel, phase 3 right panel*) are plotted per passage. (Fig. S6). **C) Exploration of the fitness landscape for the three phases of SBT** - *phase 1 (left)*: a previously adapted population (lower peak on left fitness landscape) is partitioned into smaller subpopulations. *phase 2 (middle)*: small sub-populations adapt in isolated conditions where selection pressure is reduced, allowing an extended exploration of the fitness landscape. *phase 3 (right)*: subpopulations migrate, mix and compete, evolving new and more fit variants that were explored in isolation (highest peak). Haplotype legend: A: E296K, B: D385G, C: T301I, D: A382V.

In stark contrast with the bulk experiments, amplification and hence growth of potential escape variants that sweep the population is precluded when each variant is confined in a single drop with just two host cells; as a result, the *wt* remains the dominant fraction of the observed viruses through all passages. Potential escape viruses are present, but are in complete isolation from each other, at population sizes of just a single infection event per generation. This microfluidic experiment (Fig. 1B) implements the first two phases of the shifting balance theory (Wright, 1931): i) partitioning the population in drops to weaken selection and increase genetic drift and ii) evolving the sub-populations without competition between drops. However, the absence of competition precludes detection of potential escape variants. To overcome this, we break the emulsion after five passages in the evolution chip, mix the contents of all the drops and propagate the sample in the presence of Ab under bulk conditions for three additional passages (Koonin and Wolf, 2010). This enables new escape variants that evolved in isolation to take over the integrated population and facilitates their identification, isolation and characterization. This also implements the third phase of the shifting balance theory: iii) mixing the subpopulations back into a large population. Remarkably, after mixing, a double mutant, D385G-A382V (*BD*), sweeps the population; (Fig.1B) this is in sharp contrast with the standard bulk cultures where the triple mutant *ABC* sweeps the population.

Next, we determine if the escapees in drops are more fit than the escapees in bulk. To address this question, we engineered the mutations into the infectious clone and recovered mutant viruses. Next, we performed head-to-head competition of *wt*, *BD*, and *ABC* variants. We show in Figure 2 the frequency of each of the three clones at the end of the competition. Indeed, *BD* and *ABC* are true escape variants since they outcompete *wt* under neutralizing antibody. However, without antibody, *wt* is more fit than both *BD* and *ABC*, which explains the observation that neither *BD* nor *ABC* spontaneously arise in serial passaging without Ab. More importantly, in the competition between *BD* and *ABC*, we find that the escapee from droplets is more fit compared to the escapee from bulk (Figure 2). Despite being more fit, *BD* is not detected in any of the bulk serial passaging under neutralizing Ab, while *ABC* was observed thrice. We hypothesize that the initial acquisition of the mutation D (enroute to *BD*) is limited in large populations, because epistatic interactions dictate that the virus traverse a low fitness regime, before climbing up a local fitness peak. Indeed, such unlikely pathways on the landscape can be accessed if selection is weakened by decreasing population size as Wright originally envisioned.

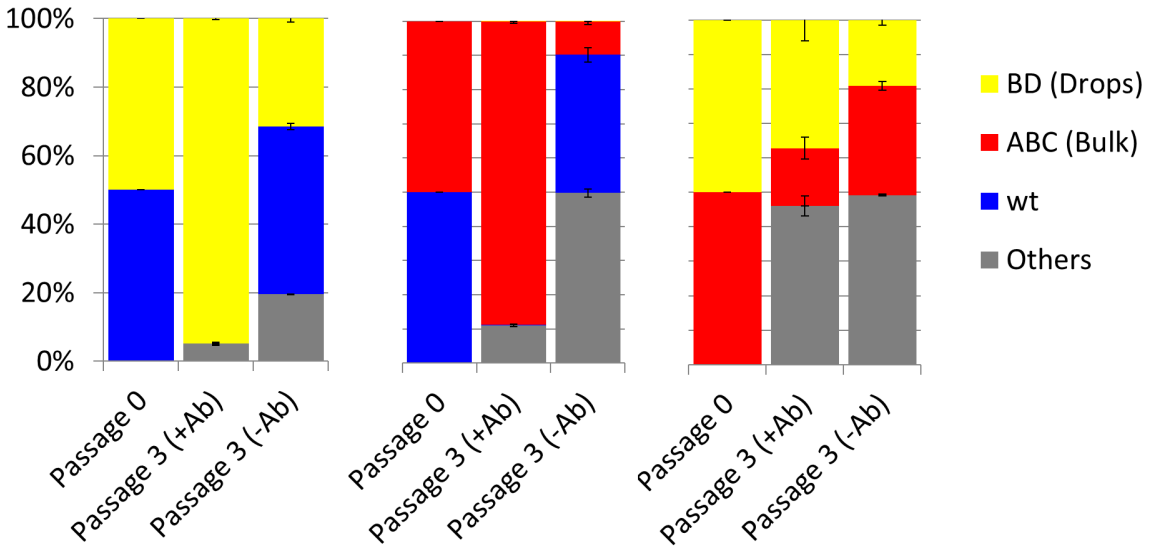

Figure 2. Allele frequency of the clone after 3 passages in competition assays. To perform pairwise competition of the clones, we mixed equal titers of the clone, propagate them for 3 passages, and then perform deep sequencing. Error bars are SE of 3 biological replicates for each measurement. See also Table S3.

These results provide strong qualitative support to Wright's shifting balance theory showing that the evolutionary dynamics and outcome dramatically depend on the population structure. To understand these dynamics quantitatively we must first develop a tractable model for the fitness landscape of the virus. In general, fitness is expected to be a complex function of multiple traits. Instead we focus on the dependence of viral fitness in the presence of a neutralizing antibody on two biophysical properties of the P-domain: The folding energy, which is a measure of stability, and the binding affinity to the antibody, which is a measure of neutralization. While the importance of binding affinity to antibody is apparent, the universal importance of protein folding stability for bacterial and viral fitness was also shown (Gong et al., 2013; Rodrigues et al., 2016). This choice of variables is further supported by the fact that all the mutations of the dominant escape variants we observe in our experiments are located within the binding site between the P-domain and the Ab, as shown by mapping the mutations on the 3D structure of the *wt* P-domain in Fig. 3A.

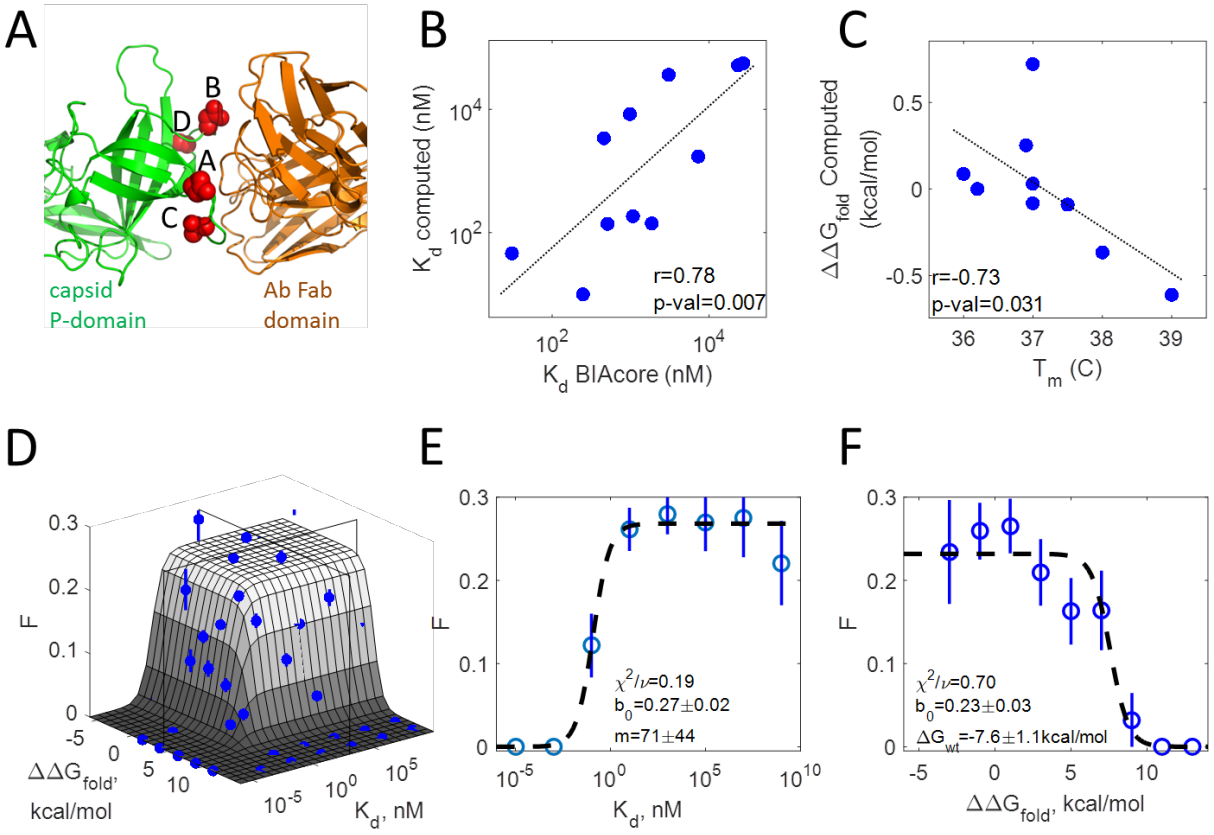

Figure 3. Fitness landscape of norovirus escaping a neutralizing antibody. A) The P-domain Antibody complex structure. The SNPs of all dominant P-domain variants (red circles) are located on the docking site of the P-domain-antibody complex (PDB ID: 3LQE). **B)** A high correlation exists between Ab dissociation constant K_d that was experimentally measured using BIAcore and the one computed from force field calculations **C)** The anti-correlation between the experimentally measured P-Domain melting temperature (T_m) and the folding stability computed from force field calculations. Two outlier variants were excluded from the analysis. **D)** A 3D plot of the probability of infection F averaged over 2,076 distinct haplotypes binned according to their dissociation constant K_d and folding stability ΔG_{fold} (blue points) overlaid with the theoretical fit according to Eq. 1. (gray surface). Cross sections (black frames) demark the regions used for the projections in B and C. **E)** The probability of infection for all haplotypes with ΔG_{fold}<4.5Kcal/mol (cross section parallel to K_d axis in A) is projected on the K_d-F plane, binned according to their K_d (blue points) and overlaid with the theoretical fit to Eq. 1. (dashed line). **F)** The probability of infection for all haplotypes with K_d>10^3nM (cross section parallel to ΔG_{fold} axis in A is projected on the ΔG_{fold}-F plane, binned according to their ΔG_{fold} (blue points) and overlaid with the theoretical fit to Eq. 1. (dashed line). F is determined from deep sequencing lysates of *in vitro* experiments in the presence of neutralizing antibody. K_d and ΔG_{fold} are estimated from mapping the haplotype mutations to the 3D structure of the capsid P-domain in complex with the neutralizing antibody. See also Fig. S5, S7.

To calculate the folding energy of the P-domain and its binding affinity to the antibody for each haplotype sequence, we use force field calculations based on the structural mapping in Fig. 3A(Koonin and Wolf, 2010; Yin et al., 2007) to determine the change in folding energy $\Delta\Delta G_{fold}$ between the mutant and the *wt*; from this we determine ΔG_{fold} of the mutant by adding the folding energy of the *wt*, ΔG_{wt}. We also determine the change in binding energy, $\Delta\Delta G_{bind}$, between the mutated P-domain-Ab complex and the *wt*; from this we determine the dissociation constant $K_d = K_0 \exp(\beta\Delta\Delta G_{bind})$ where K_0 is the dissociation constant of the *wt*. We test the accuracy of our calculations by comparing the calculated biophysical properties of the escape haplotypes to experimentally measured properties. To accomplish this, we express and purify the P-domain of each haplotype(Wolf et al., 2009) and measure its binding to the Ab to extract K_d; we also measure the melting temperature of the P-domain, T_m, which correlates inversely to ΔG_{fold}. (Table S2 and (Privalov, 1979)). The measured values of the biophysical properties of the dominant escape haplotypes correlate strongly with the calculated values of the same haplotypes, as shown in Fig. 3B and C. Importantly, we reverse engineer the escape viruses with their haplotype sequences on the background of the *wt* for the rest of the virus and confirm that the observed mutations in the P-domain are directly responsible for their increase in fitness both *in vitro* (Fig. 4A and S4) and *in vivo* in mice (Fig. 4B and S4); thus, our biophysical variables are relevant for viral fitness inside the real animal host.

The biophysical fitness landscape describes the dependence of viral fitness in the presence of a neutralizing antibody on ΔG_{fold} and $1/(mK_d)$, where the parameter m accounts for the multiple binding sites of the capsid. To formulate the viral fitness we assume that the *wt* P-domain occurs in three specific states: folded and unbound, folded and bound, and unfolded (which is always unbound). The virus infects only when the P-domain is folded and unbound, hence, we can express the viral infectivity F at a given concentration of antibody $[Ab]$ as (Cheron et al., 2016):

$$F = b_0 \frac{e^{-\beta\Delta G_{fold}}}{1 + e^{-\beta\Delta G_{fold}} + \frac{[Ab]}{mK_d} e^{-\beta\Delta G_{fold}}}, \qquad \text{(Eq. 1)}$$

where the numerator is the Boltzmann probability of being folded and unbound and the denominator is the partition function that sums over the probability of all three states, and

$\beta=1/k_BT$ where k_B is the Boltzmann constant and T is the temperature. The function F has two regimes as shown by the surface in Figure 3D. For low binding affinities and stable P-domain structures, viruses are expected to infect host cells at some fixed probability, $0<b_0<1$, determined by the average effect of all remaining viral properties on the infection process, and $F=b_0$. By contrast, when the binding to the Ab is strong or when the P-domain is unstable, the virus cannot infect its host and $F=0$.

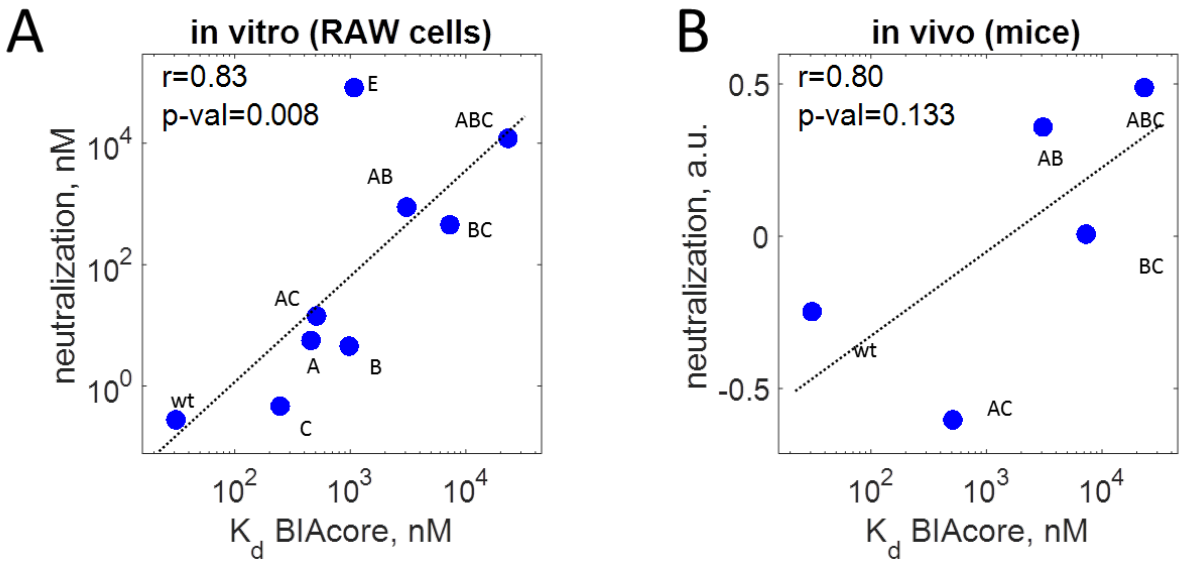

Figure 4. A) *in vitro* neutralization of dominant haplotypes correlates to their K_d and the average ratio between them is ~120, in good agreement with the modeled value of $m\approx70$. E: L386F **B)** *in vivo* neutralization of dominant haplotypes in mice correlates to their K_d.

To compare the model to experiment, we use sequencing data to determine the growth rate of each virus from the change in genome haplotype frequencies between successive generations (Acevedo et al., 2014). The growth rates distribute into two distinct groups with 87% of haplotypes exhibiting little or no growth and the rest exhibiting considerably larger growth. We take the first group to be non-infective, and take the second group to be infective ((Koonin and Wolf, 2010) and Fig. S5). For each haplotype sequence, we map the mutations to the 3D structure of the *wt* P-domain (Koonin and Wolf, 2010; Yin et al., 2007) and use Eris force field calculations to determine the change in folding energy $\Delta\Delta G_{fold}$ between the mutant and the *wt*; from this we determine stability of the mutant $\Delta G_{fold}=\Delta G_{fold,wt}+\Delta\Delta G_{fold}$, where ΔG_{wt} is the folding energy of the *wt*. We also determine the change in binding energy, $\Delta\Delta G_{bind}$, between the mutated

P-domain-Ab complex and the *wt*; from this we determine the dissociation constant $K_d=K_0e^{\beta\Delta\Delta G_{bind}}$ where K_0 is the dissociation constant of the *wt*. We bin the haplotypes using $\Delta\Delta G_{fold}$ and K_d and calculate F for each bin from the fraction of infective haplotypes. This binning exploits the large number of unique haplotypes to reduce the effects of errors in the calculations and of contributions from other biophysical properties. We fit the model by varying the three unknown parameters, b_0, ΔG_{wt} and the multiplier m.

We obtain excellent agreement between the model and the data, as shown by the dashed line in Figure 3E and F. The infectivity of haplotypes is zero at low K_d or high ΔG_{fold}, while at high K_d and low ΔG_{fold}, the landscape plateaus at F~0.25 independent of either of the biophysical coordinates. The value of $1/m$≈1.4% obtained from the fit reflects the fact that only about 3 of the 180 P-domains on the capsid have to be blocked by the Ab to prevent infection ((Fischer et al., 2015) and Fig. 3E). The value of F *~0.25* at the plateau is significantly less than the expected value of b_0=1; this points to the role of factors not included in the model, such as the interaction of the capsid with the host-cell receptor, in successful infection. Thus, binding and folding energies are very good predictors of viral extinction; however they are less successful in predicting infectivity. This suggests that antibody escape and folding stability of the capsid protein are necessary but not sufficient for viral infection.

To determine how the virus evolves on the fitness landscape, we use population genetics theory and calculate the ratio dN/dS, where *dN* is the rate of non-synonymous evolutionary rate and *dS* is the synonymous evolutionary rate (Yang and Nielsen, 2002) (see Supporting online text for details). As a rule, mutants affect the population more in regions where non-synonymous mutations are beneficial (high dN/dS), driving it down the gradient of dN/dS towards regions where non-synonymous mutations are deleterious (low dN/dS) and thus do not affect the population. The dN/dS ratio is a function of population size and of the fitness effect of a mutation or the selection coefficient $s=(F_{mutant}-F_{widltype})/F_{widltype}$ (Swanson et al., 2003; Yang and Nielsen, 2002). Using the fitness landscape from Equation 1, we calculate the dN/dS ratio on the viral fitness landscape and how it depends on population size (see Methods and (Dasmeh et al., 2014; Serohijos et al., 2012) for details). In large population sizes, dN/dS exhibits a strong gradient towards high K_d and high folding stability (Fig. 5A). Consequently, a *wt* population that is initially unstable and neutralized by Ab is expected to evolve resistance by increasing both K_d

and stability. However, in small population sizes the gradient of dN/dS is directed only towards high K_d and the same initially unstable population will evolve resistance to Ab without increasing folding stability (Fig. 5B).

The effect of population size on the course of evolution can be explained by analyzing the balance between selection and mutational drift, the two forces driving evolution. The direction of drift and selection along the trait of folding stability and binding affinity to the antibody can be inferred from protein engineering and systematic studies on effects of random mutations on proteins. Along the axis of folding stability ΔG_{fold}, beneficial mutations increase folding stability, but random de novo mutations in proteins tend to decrease stability(Kumar et al., 2006; Moal and Fernandez-Recio, 2012; Tokuriki et al., 2007; Zeldovich et al., 2007). Thus, selection and drift act in opposite directions (Fig. 5A and B, arrows), leading to mutation-selection balance. Along the axis of binding affinity K_d, beneficial mutations for the virus lead to escape from Ab (towards high K_d), and random mutations on protein interfaces perturb binding (also towards high K_d). Thus, selection and drift act along the same direction (Fig. 5A and B, arrows).

To validate the difference in expected pathways to antibody resistance based on population size, we simulate the trajectory for 4 sequential fixations of a single mutation starting from the position of the *wt* virus population on the viral fitness landscape (see (Cheron et al., 2016) for details). For large N, the simulations show that the norovirus population increases both its folding stability and dissociation constant, K_d, as it escapes the neutralizing antibody, following the trajectory shown by the solid points in Figures 4A (see also Fig. S6). After 4 sequential single mutations the model shows a rise of 5 orders of magnitude in K_d and an increase of 3kcal/mol in ΔG_{fold} towards stabilization corresponding to a change of 9°C in T_m. On the other hand, for small N the simulations show that the norovirus population increases its K_d to escape the antibody but exhibits only a small change in folding stability of less than 1kcal/mol, corresponding to an increase in T_m of about 2°C, as shown by the trajectory in Figure 5B (see also Fig. S6).

To compare the theory to experiment we plot the position of viral haplotypes evolving in 5 independent bulk passaging experiments as a function of K_d and T_m, denoting their frequencies by the size of the circles for each passage. To that end we include the calculated biophysical

values K_d and T_m (gray haplotypes), using the correlation curve in Fig. 3B to relate between ΔG_{fold} and T_m, as well as the biophysically measured values for select haplotypes (colored symbols). There is a clear trajectory as the intermediate variants evolve, having increasingly weaker affinities and higher T_m, with the escape variants at passage 5 ultimately having the weakest affinity, with an overall average of K_d ~3,000 nM and the highest P-domain stability with an average of T_m~43.5°C, as shown in Figure 5C. We also plot the position of viral haplotypes evolving in ~2 million independent drop passaging experiments. We observe a clear trajectory of increasingly weaker affinities while maintaining original T_m, with the escape variants at passage 5 ultimately having an overall average of K_d ~300 nM and T_m~36.8°C, as shown in Figure 5D. The direction of these trajectories parallels that of the simulated trajectories, supporting our choice of these explicit biophysical properties as valid and useful coordinates for the fitness landscape. This also provides us a theoretical framework with which to interpret new experimental data and to test fundamental concepts of evolutionary theory.

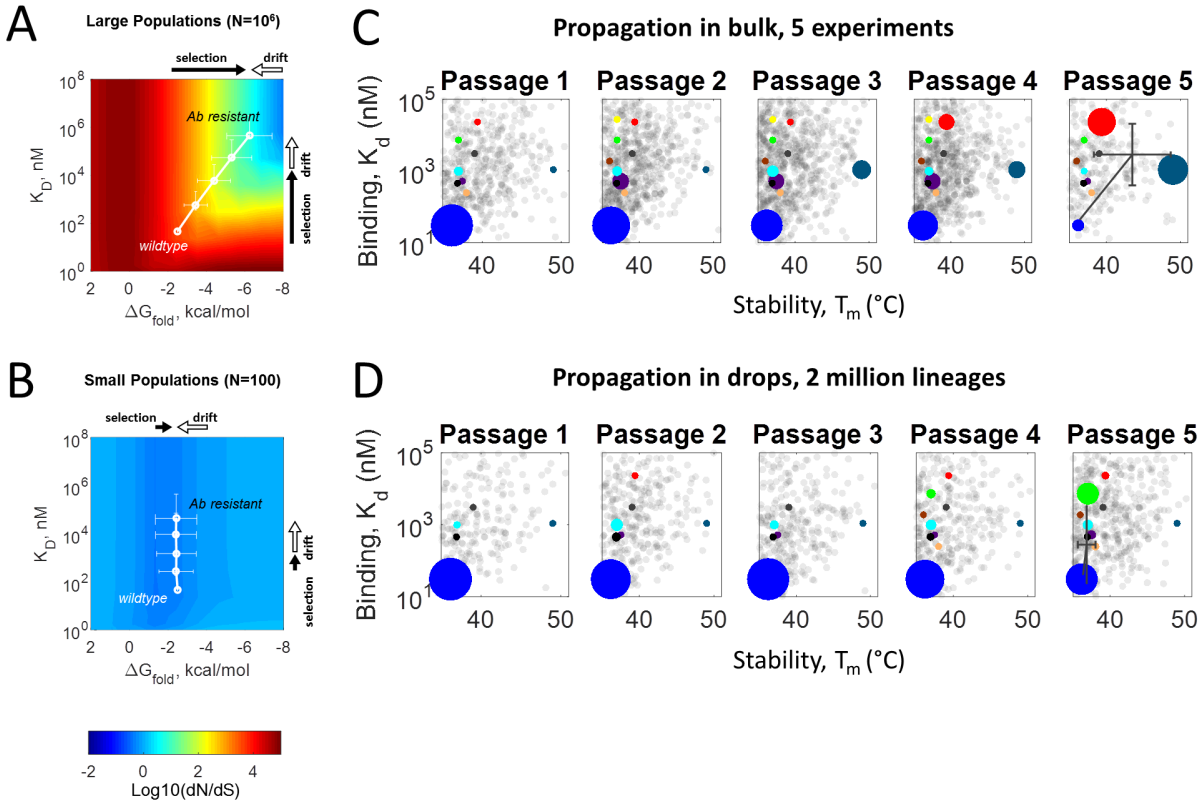

Figure 5. Most likely pathways on the fitness landscape predicted by protein biophysics and population genetics. A,B) Average stringency of selection for several population sizes (see Text and). For large population sizes, the increase in K_d is strongly coupled to the increase

in T_m. However, for small population sizes, the selection for K_d is decoupled from the selection for folding stability. The white lines are the predicted trajectories from forward evolutionary simulations of an MNV population escaping an Ab, but with a P-domain which is unstable. Each trajectory is the average of 1000 independent simulations. The direction of selection (black arrows) is towards greater folding stability and weaker affinity to the antibody. Selection is strong when the P-domain is unstable and/or is tightly bound to the Ab. Selection pressure is approximately zero when the fitness landscape is flat (neutral). Along the direction of folding stability, most random mutations are destabilizing which lead to a mutational drift (white arrows) towards protein destabilization. Along binding affinity axis, most random mutations perturb the protein-protein interaction which leads to a mutational drift towards weaker binding. **C,D)** Density plots of all haplotypes grouped according to passages. Color circles denote dominant haplotypes whose biophysical properties were measured, while the remaining gray circles denote haplotypes whose biophysical properties were calculated. The size of the circle codes for the allele frequency of each haplotype. Gray cross at passage 5 denotes mean and s.d. of all haplotypes.

DISCUSSION

It is a central concept in evolutionary biology theory that the population size determines the balance between two evolutionary forces, selection and mutational drift (Lynch and Conery, 2003; Serohijos et al., 2012). The results presented here provide direct experimental evidence in support of this central concept. Moreover, the role of Wright's shifting balance theory in real evolution has been contentious and controversial (Crow, 2008) because of lack of direct experimental demonstration. Using the segregation in the Evolution Chip, we show that isolated viral populations starting at a fitness valley in the presence of a neutralizing Ab are able to explore unlikely pathways on the adaptive fitness landscape and, following migration, shift the whole population to new fitness peaks (Fig. 1C); this is a direct demonstration of the shifting balance theory.

The ability to change the course of evolution using the Evolution Chip and to predict its direction on the biophysical fitness landscape with the parameters of protein stability and binding may be helpful in addressing pandemics. These biophysical parameters are more generally applicable to other viruses; for example, both binding (Fonville et al., 2014) and folding stability (Gong et al., 2013) are relevant traits for the evolution of an influenza virus in the presence of a neutralizing antibody. Prediction of future diversification of circulating viral mutants, is key to developing and potentially fielding an effective vaccine prior to, or in the early stages of a pandemic. The

methodology presented here may assist in proactive exploration of viral diversification to inform selection of novel viruses prior to their natural emergence, for developing viral therapeutics.

MATERIALS AND METHODS

Microfluidic devices:

We fabricate polydimethylsiloxane (PDMS) devices using photolithography and coat them with fluorophilic Aquapel (Rider, MA, USA) to prevent wetting of drops on the channel walls. Electrodes are fabricated on chip using low melting temperature solder (Mazutis et al., 2013). The designs used to fabricate the devices are available in ACAD format (Supplementary File 1). We use OEM syringe pumps (KD Scientific, MA, USA) to drive the fluidics and a fast camera (HiSpec1, Fastec Imaging,USA) to image encapsulation and drop fusion.

Reagents

For the inert carrier oil we use HFE-7500 (3M, USA) with 1% w/w of a block co-polymer surfactant of perfluorinated polyethers (PFPE) and polyethyleneglycol (PEG)(Holtze et al., 2008). A compatible surfactant is available commercially (008-FluoroSurfactant, Ran Biotechnologies, USA). To separate the emulsion, we use a commercially available demulsifier (1H,1H,2H,2H-perfluoro-1-octanol, CAS # 647-42-7). Other chemicals were purchased from Sigma Aldrich (St. Louis, MO).

Clones and Antibodies

The plaque-purified MNV-1 clone (GV/MNV-1/2002/USA) MNV-1.CW3 (Thackray et al., 2007) (referred herein as *wt*) was used at passage 6 for in vitro passaging experiments. Recombinant MNV-1 viruses containing P-domain point mutants E296K (*A*), D385G (*B*), T301I (*C*), A382V (*D*), L386F (*E*), E296K-T301I (*AC*), E296K-D385G (*AB*), T301I-D385G (*BC*), A382V-D385G (*BD*) and E296K-T301I-D385G (*ABC*) were generated as previously described (Kolawole et al., 2014b). The isotype control IgG directed against Coxsackievirus B4 (CV) (clone 204-4) was purchased from ATCC (HB 185). Anti-MNV-1 monoclonal antibody (mAb) A6.2 (IgG2a) was grown in Bioreactor CELLine CL 1000 flasks (Sigma-Aldrich) following the manufacturer's recommendations. Antibodies were purified over a HiTrap protein A column (GE Healthcare) according to the manufacturer's instruction, dialyzed against PBS, and stored at -20 °C.

MNV-1 P-domain mutant expression and purification

All recombinant proteins was expressed and purified as previously reported (Taube et al., 2010) with some modifications. Briefly, the P domain of MNV-1 (residues 225 to 541) was cloned into a pUC57 expression vector with NH2-terminal 6-histidine tag. The protein was expressed overnight at 20°C in Escherichia coli. The cells were subsequently lysed, and the protein was obtained from the supernatant, two steps purification by Ni column and by gel filtration on a Superdex 75 column (GE Healthcare). The proteins were dialyzed overnight at 4°C against a phosphate buffer (pH=7.8 and 20 mM NaCl).

Folding stability using thermofluorescence

Thermal denaturation was carried out using melt-curve module of BioRad CFX96, and Sypro Orange dye as a probe for unfolding as described earlier (Niesen et al., 2007). The dye was added to the final concentration of 5× in a 25 µl reaction volume containing 4 µM of protein in 10 mM sodium phosphate buffer pH 7.8. To control for concentration dependence, we also performed the experiment using 2 µM concentration of protein. The T_m is estimated as the extremum of the derivative of the fluorescence signal. We report the average T_m of eight technical repeats, four for 4 µM of protein and another four for 2 µM of protein.

Binding kinetics using surface plasmon resonance

Realtime biomolecular analysis was performed by surface plasmon resonance (SPR) using a BIAcore 3000 instrument equipped with nitrilotriacetic acid (NTA) sensor chip. Purified monoclonal antibody A6.2 was immobilized on the surface while the MNV-1 P-domain variants were the analytes. To perform single kinetic measurement, we (1) Quickinjected 20 µl of buffer (10 mM sodium phosphate buffer pH 7.8 with 0.005% surfactant to prevent minimizing non-specific interaction); (2) Kinjected 50 uL of protein with 100 s dissociation; (3) Quickinjected 10 µl of regeneration buffer (pH 2.0); and (4) Quickinjected 20 µl of phosphate buffer. For each MNV variant, we performed kinetic measurements with concentrations in the range of 0.5 to 100 µM. Data analysis was conducted with BIAevaluation package. Curve fittings were done with the 1:1 Langmuir binding model.

Cell Culture

RAW 264.7 (murine macrophage) cells were purchased from ATCC (Manassas, VA) and maintained as described previously (Taube et al., 2010; Wobus et al., 2004). Adherent cell culture medium (RAW medium) contains Dulbecco's Modified Eagle's Medium, 4 mM L-glutamine, 100 µg/mL penicillin, 100 µg/mL streptomycin, 10 mM HEPES, 10% heat-

inactivated fetal bovine serum. The RAW 264.7 were adapted to suspension culture in spinner flasks for these experiments, for compatibility with drop-based microfluidics. Suspension cell culture medium (Suspension Medium) contains adherent RAW medium supplemented with sodium bicarbonate (7.5%). BSRT7 (BHK cells expressing T7 polymerase) cells were cultured in DMEM supplemented with 10% heat-inactivated fetal bovine serum, 2 mM L-glutamine, 100 U/ml penicillin and 100 µg/ml streptomycin(Buchholz et al., 1999). For all viral infection experiments, suspension RAW 264.7 cells were suspended in Enhanced Suspension Medium (ESM) comprised of Suspension Medium supplemented with 15% optiprep.

Viral evolution in bulk

RAW 264.7 suspension cells are centrifuged for 5 min at 3,000 rpm and re-suspended in fresh medium at a concentration of $6x10^6$ cells/mL. In antibody neutralization experiments, virus is first incubated for 30 min at 37°C with mAb A6.2 in 200 µL PBS prior to dilution into ESM at $4x10^6$ pfu/mL, such that the final Ab concentration is 8.57 nM. One mL of cell suspension and 1 mL of virus suspension are mixed in a single well of a 12-well dish containing a sterile stir bar and incubated on stir plate in a 37°C incubator, 5% CO2, for 24 hrs. To passage viral progeny to the next generation (the progeny of the first inoculum is considered passage 0 (P0)), 250 uL of the supernatant from cell lysates of the previous generation is supplemented to 2 mL of a fresh suspension of $2x10^6$ RAW cells/mL in ESM in a 12-well dish containing a sterile stir bar and incubated on the stir plate in a 37°C incubator, 5% CO2, for 24 hrs. In antibody neutralization experiments, 8.57 nM mAb A6.2 is supplemented to the fresh suspension of RAW cells prior to passaging. Cell lysates were harvested by 2 rounds of freeze/thaw and centrifugation for 5 min at 5,000 x g.

Viral evolution in drops

To evolve viruses in small population sizes we use a novel microfluidics system, the "Evolution Chip", which propagates ~10^6 subpopulations of 1-10 infectious particles (pfu) in distinct and non-mixing compartments. We encapsulate ~2 host cells and ~1 pfu in 100µm diameter aqueous drops in inert oil at a rate of millions per hour. The resultant emulsion is incubated under physiological conditions for one viral life cycle (~24 hours). Successful replication of the virus leads to the death of the host cell and the release of viral progeny within the drop. Thus, to enable continued passage, each drop is split and ~10% of its volume, containing viral progeny from the previous generation, is merged with a new drop containing a fresh host cell for the next generation.

Suspension-adapted RAW 264.7 cells were centrifuged for 5 min at 3,000 rpm, re-suspended in ESM at $8x10^6$ cells/mL. The suspension of cells is co-flowed at a 1:1 ratio with MNV-1 virus diluted into ESM at $4x10^6$ pfu/mL. The two aqueous phases - cell suspension and buffer - meet immediately before passing through the microfluidic drop making junction so that they only mix inside the 100um drops containing them (Supplementary Movie 1). For the continuous phase dispersing the drops, we use HFE-7500 Oil with 1% surfactant. Typical flow rates are 8 mL/hr for the oil and 2 mL/hr for cells and virus. Drops were collected in 1.5 mL tubes and incubated at 37°C, in 5% CO2. Following 18-24 hr incubation at 37°C, drops are re-injected into the "evolution-chip" microfluidic device where ~10% of their volume is split off and fused with freshly formed drops containing freshly prepared suspension of RAW cells in ESM. The synchronization in the device ensures that in >95% of cases, the split from one drop fuses with exactly one newly formed drop, enabling the viral lineages to propagate in isolation. Typical flow rates are 4 mL/hr for the oil, 1 mL/hr for the re-injected drops, and 1 mL/hr for the fresh cells. The newly formed drops are collected in 1.5 mL tubes and incubated at 37°C, in 5% CO2, while the content of the old, split drops are extracted for analysis (The progeny of the first encapsulation is considered passage 0 (P0)). In antibody neutralization experiments, 8.57 nM mAb A6.2 is supplemented to the fresh suspension of RAW cells prior to re-injection of drops.

Head to head competitions between viral strains

Next, we determine if the escapees in drops are more fit than the escapees in bulk. To address this question, we performed head-to-head competition of *wt*, *BD*, and *ABC* strains. We mixed equal viral titers of each pair of strains, passaged them for 3 rounds and then performed deep sequencing. The competition was performed under two conditions, with and without neutralizing antibody, and over three replicates. The sequencing results of the competitions are given in Table S3.

RAW 264.7 suspension cells are centrifuged for 5 min at 3,000 rpm and 2 mL of a fresh suspensions of $1x10^6$ RAW cells/mL in RAW medium is dispensed in 6-well plates. In antibody neutralization experiments, virus is first incubated for 30 min at 37°C with mAb A6.2 in 200 µL PBS prior to adding it into the wells, such that the final Ab concentration is 0.08 nM. Cells and virus are incubated in a 37°C incubator, 5% CO2, for 48 hrs. To passage viral progeny to the next generation (the progeny of the first inoculum is considered passage 0 (P0)), 200 uL of the supernatant from cell lysates of the previous generation is supplemented to 2 mL of a fresh suspension of $1x10^6$ RAW cells/mL in RAW medium in a 6-well dish and incubated in a 37°C incubator, 5% CO2, for 24 hrs. In antibody neutralization experiments, 0.08 nM mAb A6.2 is supplemented to the fresh suspension of RAW cells prior to passaging. Cell lysates were harvested by 2 rounds of freeze/thaw and centrifugation for 5 min at 5,000 x g.

In-vitro neutralization measurements

To measure neutralization in-vitro we followed Fischer et. al (Fischer et al., 2015) to obtain a neutralization curve which we then fit by the equation: $y = \frac{1}{1+\frac{K_d}{X}}$ where y is the viral titer, X is the Ab concentration and k_d is the fitting parameter.

In-vivo neutralization measurements

Mouse studies were performed in accordance with local and federal guidelines as outlined in the "Guide for the Care and Use of Laboratory Animals" of the National Institutes of Health. Protocols were approved by the University of Michigan Committee on Use and Care of Animals (UCUCA Number: 09710).Viral strains were neutralized in $STAT^{-/-}$ mice injected with 500ug mAb A6.2 and compared to their infection in mice injected with an isotype as described in (Kolawole et al., 2014a). The decrease in viral titers was first standardized for each tissue across viral strains, before the average over all tissues within each strain was taken as its final neutralization score. The study was performed in biological triplicates. No randomization or blinding was used.

Measurement of infectious virus titer

Viral titer was determined by either plaque assay, as described previously(Gonzalez-Hernandez et al., 2012), or by TCID50 assay, as described previously (Arias et al., 2012). TCID 50% infectivity was translated to plaque forming unit (pfu) using the conversion of 0.7 TCID50 units to 1 pfu.

Quantification of viral genome

Viral RNA isolated from experimental samples by MagMAX Viral RNA Isolation Kit (Life Technologies) was evaluated by qPCR using MNV-1-specific primer/probe sequences (Forward: GTGCGCAACACAGAGAAACG, Reverse: CGGGCTGAGCTTCCTGC, and probe: FAM/CTAGTGTCTCCTTTGGAGCACCTA/TAMARA) (Taube et al., 2010). Takara One Step reagent (Mountain View, CA) was used to measure the genome copy of viral samples. qRT-PCR was performed on ABI real time PCR machine (OneStep Plus) using the following thermal cycling parameters: 5 min at 42° C and 10 sec at 95° C, 40 cycles of 5 sec at 95° C and 34 sec at 60° C. Titered MNV-1 viral stock and PicoGreen (quBit)-quantitated pT7 MNV 3'RZ plasmid

(Arias et al., 2012) were used as standards for pfu/mL and genome copies/mL analysis, respectively.

Amplicon preparation and sequencing

Viral RNA was isolated using the MagMax viral RNA kit (Life Technologies), then subjected to DNAse digest using DNAfree Turbo DNAse (Life Technologies). SuperScript III reverse transcriptase (Life Technologies) was then used to convert vRNA to first strand DNA with specific primers tiling the entirety of MNV-1 at ~1kb increments using the following primers:

AGCCGATCACAGGCTCCTTGGC

CCATGTTGGATAAGAGGGCTGGC

ACGCACTTCCTCAACTCAGCCG

GGCCATGCTGATCCTGGCCA

CCACCAGGATGCCATCCGAGA

GTCGACATCAGCGCGTGGTATGA

CAACAGGGTGGGCACCACGTC

CAACAACAGGGCTCTCAGCATAAACCAG

Library preparation for Illumina sequencing on the miSeq platform was carried out in accordance with Illumina tech note 15044223 Rev. A using KAPA HotStart HiFi DNA polymerase 2x master mix (KAPA Biotechnologies), with primers for MNV-1 capsid amplification corresponding to MNV-1 VP1 nucleotides 848-1275 (Forward: TCGTCGGCAGCGTCAGATGTGTATAAGAGACAG(***GTTCATGGGTGTCCTGCTTT***), Reverse: GTCTCGTGGGCTCGGAGATGTGTATAAGAGACAG(***GGGGAGAAAGGGACCAATT***); gene specific portion in bold/italic/parentheses). After purification with Ampure XP (Beckman Genomics), samples were quantified using Qubit high sensitivity reagents (Life Technologies), then pooled in equimolar ratios assuming specific amplification during adapter addition. Final pools of up to 96 libraries were quantified using high sensitivity Bioanalyzer reagents (Agilent) prior to sequencing 2X250 bp long paired end reads of the amplicons with miSeq (v2 chemistry, miSeq control software v2.3.0.3). Samples were supplemented with 10% phiX control library (Illumina). All reagents were used according to manufacturer's recommendations, and obtained from Life Technologies unless otherwise noted.

Amplicon sequencing analysis

Paired end reads were obtained from the MiSeq after going through the MiSeq Reporter Generate FASTQ Workflow, which demultiplexes the raw data by MID pair (removing adapter sequences in the process), and creates a separate pair of output files for each paired-end sample. These paired-end reads are aligned to the MNV-1 reference sequence (RefSeq: NC_008311) using bowtie2 (http://bowtie-bio.sourceforge.net/bowtie2/) and only reads that include the amplicon range (nucleotides 5918 to 6293 of MNV-1) without insertions and deletions are analyzed. SNPs in each of the remaining reads are saved for further analysis together with their Illumina reported quality. SNPs in overlapping regions of the paired end reads are called using the read with the higher quality. If the call in both forward and reverse reads match, the quality of SNP is taken as the sum of qualities, otherwise, the difference between the higher and lower quality is taken. Sequences with more than 20 substitutions were discarded and the remaining reads were then clustered into unique candidate haplotypes and tested for statistical significance using a hypothesis test. The null hypothesis presumed that a haplotype candidate is generated by sequencing errors in the reading of one of its "potential ancestors". Potential ancestors are haplotypes that are both "nearest neighbors" - have the smallest hamming distance to the candidate - and are more frequent - have more reads than the candidate. We used a simple generative model using a base-calling substitution rate equal to the lowest read quality recorded for any of the relevant substitutions in the candidate reads and then calculated the probability that the observed candidate was derived from this distribution (see determination of significance).

Determination of significance from sequencing

Initially, the most abundant haplotype is assigned p-value=0. Haplotypes are tested in descending order of their frequency. For each haplotype, a group of "potential ancestor haplotypes" was defined as those haplotypes that are both "nearest neighbors" - have the smallest hamming distance to it - and are more frequent - have more reads than this haplotype. The single event probability that a copy of the candidate haplotype was generated while sequencing a copy of each potential ancestor is calculated using the quality of reads of the nucleotides that differ between the two haplotypes: the score for each substitution address was calculated as the lowest quality over all reads sequenced in that address for the candidate haplotype. The final score was calculated from the product of all single substitution scores. The probability P_{ij} that a candidate haplotype i was generated by sequencing errors in the reading of a potential ancestor j was determined using the complementary cumulative density (CCDF) of a binomial function, with the number of trials equal to the frequency of the potential ancestor, the number of successes equal to the frequency of the candidate haplotype and the success rate taken as the single event probability. This probability is calibrated according to the probability of ancestor P_j so that $P_{ij}' =$

1 - (1 - P_{ij})(1 - P_j). Finally, the P value of haplotype i is calculated as the maximum probability over all potential ancestors: $Pi = max_j\{P'_{ij}\}$

Calculation of probability of infection P_{infect} from growth rates

To obtain the fitness landscape in Figure 1, we define the probability of infection of each haplotype as $P_{inf} = \Theta(\rho - 10^{-3})$, where ρ is the growth rate of the haplotype calculated as described below. Applying this threshold is motivated by the fact that the distribution of growth rates is bimodal – most haplotypes are either infective to some extent (ρ>=0.1) or not (ρ=0) with less than 1% of growth rates fall within the intermediate region (see Figure S2A). Consequently, the setting of the threshold is insensitive in the region (0,0.1).

Calculation of growth rates from haplotype frequencies

We calculate growth rates by comparing between haplotype frequencies of consecutive generations. To avoid sequencing errors, we only consider frequencies with p-value$\leq 10^{-4}$. Additionally, since our growth rates are relative to that of the WT, we only use data from the first 2 passages of evolution, where the WT is still the most abundant haplotype.

For each pair of consecutive generations that were sequenced, we calculate the growth rate ρ_i of all haplotypes that were detected in the samples using a simple linear model:

$$n_i' = n_i \cdot \rho_i \qquad \text{(Eq. S1)}$$

where n_i and n_i' are the copy numbers of haplotype i in the first and second generation respectively. We ignore mutation rates since mutation rates of MNV (~10^{-4}) are smaller than the sequencing errors (~10^{-3}). Assuming unbiased sampling of original copies during sequencing, we substitute:

$$n_i = f_i \cdot \Sigma n \qquad \text{(Eq. S2)}$$

$$n_i' = f_i' \cdot \Sigma n' = f_i' \Sigma(n_i \cdot \rho_i) = f_i' \Sigma(f_i \cdot \rho_i \Sigma n)$$

where f_i and f_i' are the frequency of haplotype i measured by sequencing the first and the second sample respectively. When we use these substitutions in the original equation (1) we get:

$$f_i' \Sigma(f_i \cdot \rho_i \Sigma n) = f_i \cdot \rho_i \Sigma n \qquad \text{(Eq. S3)}$$

$$f_i' \Sigma(f_i \cdot \rho_i) = f_i \cdot \rho_i$$

the resulting set of linear equations, one per haplotype, is a homogenous system:

$$AP = 0$$

where the parameter matrix is $A_{ij} = f_i'f_j - \delta_{ij}$ and the growth rates vector is $P_j = \rho_j$.

The non-trivial solution solves for all growth rates, assuming a growth rate of 1 for the wild type.

Since the same haplotype may exist in more than one pair of consecutive generations, multiple growth rates can be assigned to the same haplotype, in which case the average growth rate is calculated for this haplotype. The distribution of all growth rates is plotted in Fig. S2A.

ACKNOWLEDGEMENTS

The authors would like to acknowledge C. Wilke and J. Plotkin for very helpful comments. This work was supported by Defense Advanced Research Projects Agency (DARPA) contract # HR0011-11-C-0093, by the National Science Foundation (DMR-1310266 to DW and MCB-1243837 to ES), NIH GM068670 (ES), by the Harvard Materials Research Science and Engineering Center (DMR-1420570) and by the National Natural Science Foundation of China (HZ, 81372496).

COMPETING INTERESTS

The authors declare none.

REFERENCES

Acevedo, A., Brodsky, L., and Andino, R. (2014). Mutational and fitness landscapes of an RNA virus revealed through population sequencing. Nature *505*, 686-690.

Arias, A., Urena, L., Thorne, L., Yunus, M.A., and Goodfellow, I. (2012). Reverse genetics mediated recovery of infectious murine norovirus. Journal of visualized experiments : JoVE.

Buchholz, U.J., Finke, S., and Conzelmann, K.K. (1999). Generation of bovine respiratory syncytial virus (BRSV) from cDNA: BRSV NS2 is not essential for virus replication in tissue culture, and the human RSV leader region acts as a functional BRSV genome promoter. J Virol *73*, 251-259.

Cheron, N., Serohijos, A.W., Choi, J.M., and Shakhnovich, E.I. (2016). Evolutionary dynamics of viral escape under antibodies stress: A biophysical model. Protein Sci *25*, 1332-1340.

Crow, J.F. (2008). Mid-century controversies in population genetics. Annual review of genetics *42*, 1-16.

Dasmeh, P., Serohijos, A.W., Kepp, K.P., and Shakhnovich, E.I. (2014). The influence of selection for protein stability on dN/dS estimations. Genome biology and evolution *6*, 2956-2967.

de Visser, J.A., and Krug, J. (2014). Empirical fitness landscapes and the predictability of evolution. Nat Rev Genet *15*, 480-490.

Ettayebi, K., Crawford, S.E., Murakami, K., Broughman, J.R., Karandikar, U., Tenge, V.R., Neill, F.H., Blutt, S.E., Zeng, X.L., Qu, L.*, et al.* (2016). Replication of human noroviruses in stem cell-derived human enteroids. Science *353*, 1387-1393.

Fischer, A.E., Wu, S.K., Proescher, J.B., Rotem, A., Chang, C.B., Zhang, H., Tao, Y., Mehoke, T.S., Thielen, P.M., Kolawole, A.O., *et al.* (2015). A high-throughput drop microfluidic system for virus culture and analysis. Journal of virological methods *213*, 111-117.

Fonville, J.M., Wilks, S.H., James, S.L., Fox, A., Ventresca, M., Aban, M., Xue, L., Jones, T.C., Le, N.M., Pham, Q.T., *et al.* (2014). Antibody landscapes after influenza virus infection or vaccination. Science *346*, 996-1000.

Gong, L.I., Suchard, M.A., and Bloom, J.D. (2013). Stability-mediated epistasis constrains the evolution of an influenza protein. eLife *2*, e00631.

Gonzalez-Hernandez, M.B., Bragazzi Cunha, J., and Wobus, C.E. (2012). Plaque assay for murine norovirus. Journal of visualized experiments : JoVE, e4297.

Guo, M.T., Rotem, A., Heyman, J.A., and Weitz, D.A. (2012). Droplet microfluidics for high-throughput biological assays. Lab Chip *12*, 2146-2155.

Holtze, C., Rowat, A.C., Agresti, J.J., Hutchison, J.B., Angile, F.E., Schmitz, C.H.J., Koster, S., Duan, H., Humphry, K.J., Scanga, R.A., *et al.* (2008). Biocompatible surfactants for water-in-fluorocarbon emulsions. Lab on a Chip *8*, 1632-1639.

Jones, M.K., Watanabe, M., Zhu, S., Graves, C.L., Keyes, L.R., Grau, K.R., Gonzalez-Hernandez, M.B., Iovine, N.M., Wobus, C.E., Vinje, J., *et al.* (2014). Enteric bacteria promote human and mouse norovirus infection of B cells. Science *346*, 755-759.

Katpally, U., Wobus, C.E., Dryden, K., Virgin, H.W.t., and Smith, T.J. (2008). Structure of antibody-neutralized murine norovirus and unexpected differences from viruslike particles. J Virol *82*, 2079-2088.

Kimura, M. (1968). Evolutionary rate at the molecular level. Nature *217*, 624-626.

Kolawole, A.O., Li, M., Xia, C., Fischer, A.E., Giacobbi, N.S., Rippinger, C.M., Proescher, J.B., Wu, S.K., Bessling, S.L., Gamez, M., *et al.* (2014a). Flexibility in surface-exposed loops in a virus capsid mediates escape from antibody neutralization. J Virol *88*, 4543-4557.

Kolawole, A.O., Li, M., Xia, C.S., Fischer, A.E., Giacobbi, N.S., Rippinger, C.M., Proescher, J.B.G., Wu, S.K., Bessling, S.L., Gamez, M., *et al.* (2014b). Flexibility in Surface-Exposed Loops in a Virus Capsid Mediates Escape from Antibody Neutralization. Journal of virology *88*, 4543-4557.

Koonin, E.V., and Wolf, Y.I. (2010). Constraints and plasticity in genome and molecular-phenome evolution. Nat Rev Genet *11*, 487-498.

Kumar, M.D., Bava, K.A., Gromiha, M.M., Prabakaran, P., Kitajima, K., Uedaira, H., and Sarai, A. (2006). ProTherm and ProNIT: thermodynamic databases for proteins and protein-nucleic acid interactions. Nucleic acids research *34*, D204-206.

Lang, G.I., Rice, D.P., Hickman, M.J., Sodergren, E., Weinstock, G.M., Botstein, D., and Desai, M.M. (2013). Pervasive genetic hitchhiking and clonal interference in forty evolving yeast populations. Nature *500*, 571-574.

Luksza, M., and Lassig, M. (2014). A predictive fitness model for influenza. Nature *507*, 57-61.

Lynch, M., and Conery, J.S. (2003). The origins of genome complexity. Science *302*, 1401-1404.

Mazutis, L., Gilbert, J., Ung, W.L., Weitz, D.A., Griffiths, A.D., and Heyman, J.A. (2013). Single-cell analysis and sorting using droplet-based microfluidics. Nature protocols *8*, 870-891.

Moal, I.H., and Fernandez-Recio, J. (2012). SKEMPI: a Structural Kinetic and Energetic database of Mutant Protein Interactions and its use in empirical models. Bioinformatics *28*, 2600-2607.

Nahum, J.R., Godfrey-Smith, P., Harding, B.N., Marcus, J.H., Carlson-Stevermer, J., and Kerr, B. (2015). A tortoise-hare pattern seen in adapting structured and unstructured populations suggests a rugged fitness landscape in bacteria. Proc Natl Acad Sci U S A *112*, 7530-7535.

Niesen, F.H., Berglund, H., and Vedadi, M. (2007). The use of differential scanning fluorimetry to detect ligand interactions that promote protein stability. Nature protocols *2*, 2212-2221.

Privalov, P.L. (1979). Stability of proteins: small globular proteins. Adv Protein Chem *33*, 167-241.

Rodrigues, J.V., Bershtein, S., Li, A., Lozovsky, E.R., Hartl, D.L., and Shakhnovich, E.I. (2016). Biophysical principles predict fitness landscapes of drug resistance. Proceedings of the National Academy of Sciences of the United States of America *113*, E1470-1478.

Sanjuan, R., Moya, A., and Elena, S.F. (2004). The distribution of fitness effects caused by single-nucleotide substitutions in an RNA virus. Proceedings of the National Academy of Sciences of the United States of America *101*, 8396-8401.

Serohijos, A.W.R., Rimas, Z., and Shakhnovich, E.I. (2012). Protein Biophysics Explains Why Highly Abundant Proteins Evolve Slowly. Cell Reports *2*, 249-256.

Swanson, W.J., Nielsen, R., and Yang, Q. (2003). Pervasive adaptive evolution in mammalian fertilization proteins. Mol Biol Evol *20*, 18-20.

Tao, Y., Rotem, A., Zhang, H., Chang, C.B., Basu, A., Kolawole, A.O., Koehler, S.A., Ren, Y., Lin, J.S., Pipas, J.M.*, et al.* (2015a). Rapid, targeted and culture-free viral infectivity assay in drop-based microfluidics. Lab on a chip *15*, 3934-3940.

Tao, Y., Rotem, A., Zhang, H., Cockrell, S.K., Koehler, S., Chang, C.B., Ung, L.W., Cantalupo, P., Ren, Y., Lin, J.S.*, et al.* (2015b). Artifact-free Quantification and Sequencing of Rare Recombinant Viruses Using Drop-based microfluidics. Chembiochem : a European journal of chemical biology.

Taube, S., Rubin, J.R., Katpally, U., Smith, T.J., Kendall, A., Stuckey, J.A., and Wobus, C.E. (2010). High-resolution x-ray structure and functional analysis of the murine norovirus 1 capsid protein protruding domain. J Virol *84*, 5695-5705.

Taubenberger, J.K., Morens, D.M., and Fauci, A.S. (2007). The next influenza pandemic: can it be predicted? Jama *297*, 2025-2027.

Teunis, P.F., Moe, C.L., Liu, P., Miller, S.E., Lindesmith, L., Baric, R.S., Le Pendu, J., and Calderon, R.L. (2008). Norwalk virus: how infectious is it? Journal of medical virology *80*, 1468-1476.

Thackray, L.B., Wobus, C.E., Chachu, K.A., Liu, B., Alegre, E.R., Henderson, K.S., Kelley, S.T., and Virgin, H.W.t. (2007). Murine noroviruses comprising a single genogroup exhibit biological diversity despite limited sequence divergence. J Virol *81*, 10460-10473.

Tokuriki, N., Stricher, F., Schymkowitz, J., Serrano, L., and Tawfik, D.S. (2007). The stability effects of protein mutations appear to be universally distributed. J Mol Biol *369*, 1318-1332.

Wobus, C.E., Karst, S.M., Thackray, L.B., Chang, K.O., Sosnovtsev, S.V., Belliot, G., Krug, A., Mackenzie, J.M., Green, K.Y., and Virgin, H.W. (2004). Replication of Norovirus in cell culture reveals a tropism for dendritic cells and macrophages. PLoS biology *2*, e432.

Wobus, C.E., Thackray, L.B., and Virgin, H.W.t. (2006). Murine norovirus: a model system to study norovirus biology and pathogenesis. J Virol *80*, 5104-5112.

Wolf, Y.I., Novichkov, P.S., Karev, G.P., Koonin, E.V., and Lipman, D.J. (2009). The universal distribution of evolutionary rates of genes and distinct characteristics of eukaryotic genes of different apparent ages. Proceedings of the National Academy of Sciences of the United States of America *106*, 7273-7280.

Wright, S. (1931). Evolution in Mendelian Populations. Genetics *16*, 97-159.

Yang, Z., and Nielsen, R. (2002). Codon-substitution models for detecting molecular adaptation at individual sites along specific lineages. Mol Biol Evol *19*, 908-917.

Yin, S., Ding, F., and Dokholyan, N.V. (2007). Eris: an automated estimator of protein stability. Nature methods *4*, 466-467.

Zeldovich, K.B., Chen, P., and Shakhnovich, E.I. (2007). Protein stability imposes limits on organism complexity and speed of molecular evolution. Proceedings of the National Academy of Sciences of the United States of America *104*, 16152-16157.

Zhang, H., Cockrell, S.K., Kolawole, A.O., Rotem, A., Serohijos, A.W., Chang, C.B., Tao, Y., Mehoke, T.S., Han, Y., Lin, J.S.*, et al.* (2015). Isolation and Analysis of Rare Norovirus Recombinants from Coinfected Mice Using Drop-Based Microfluidics. Journal of virology *89*, 7722-7734.